MOF-derived Mn/Al sulfide electrocatalysts enabling high-faradaic-efficiency water oxidation

Krishnendu M Nair, Selvadharshini K., Selvaraju Thangavelu*
Department of Chemistry, Bharathiar University, Coimbatore 641 046, India
Email: veluselvaraju@gmail.com; selvaraju@buc.edu.in

Materials

Aluminium chloride ($AlCl_3$), manganese chloride tetrahydrate ($MnCl_2.4H_2O$), thiourea (CH_4N_2S, 99−100.5 %), potassium hydroxide (KOH), N, N dimethyl formamide (C_3H_7NO) and sulphuric acid (H_2SO_4) (98 %) were obtained and used without any purification from Merck, India. 1,3,5-benzenetricarboxylic acid ($C_6H_3(CO_2H)_3$ (BTC)) and tellurium powder were purchased from Sigma-Aldrich, India. Selenium metal powder was purchased from High Purity Laboratory Chemicals, India. Stainless Steel mesh (SS mesh) (150 mesh woven from 0.066 mm dia) wire was purchased from Thermo Scientific. N-methyl-2-pyrrolidone (NMP, ≥ 99.5 %) and polyvinylidene fluoride (PVDF) were obtained from Alfa Aesar, India. Notably, all the chemicals were synthesized and further electrochemical studies were carried out using double distilled (DD) water.

XRD Calculations

The average crystallite size of the composite can be calculated using the Debye-Scherer equation:

$$D = \frac{K\lambda}{\beta Cos\theta} \quad \text{(S1)}$$

Where D is the crystallite size, K denoted the Scherrer constant (0.98), λ represents the wavelength (1.54), and the β represents the full width at half maximum (FWHM).

Electrode preparation for OER, HER and overall water splitting

The SS mesh (1 × 1 cm^2) was used as the working electrode for OER, HER, and overall water splitting. Herein, homogeneous solution was obtained by dispersing 5 mg of finely grounded nanocomposite with the mixed solution of NMP and PVDF, followed by ultrasonication for an hour. Afterwards, the obtained slurry was drop-cast on either side of the SS mesh and dried in a hot air oven at 50 °C for 12 h. Moreover, for both the HER and OER, the Ag/AgCl was used as the reference electrode. The potential obtained at the Ag/AgCl (3 M KCl) electrode was converted to the potential with respect to the Reversible Hydrogen Electrode (RHE) for HER and OER by the following Eq (S2).[1,2]

$$RHE = (0.0591 \times pH) + E_{reference} + E_{observed} \quad \text{(S2)}$$

Where $E_{reference}$ = 0.197 V.

Eq (S3) was used to calculate the overpotential for HER from the onset potential.

$$\eta = 0 - E_{observed} \quad \text{(S3)}$$

Eq (S4) was used to calculate the overpotential for OER from the onset potential.[3,4]

$$\eta = E_{observed} - 1.23\ V \quad \text{(S4)}$$

The active site density (n) can be calculated using the following expression (Eq (S5)):

$$n = {Q}/{kF} \quad \text{(S5)}$$

Where k represents the number of electrons involved in the HER and OER processes. Q is the voltametric charge, and F is the Faraday constant (96485 C/mol). 'k' value remains as 2 and 4 in the HER and OER processes. The intrinsic activity of the electrocatalyst was investigated by calculating the turnover frequency (TOF). Using this active site density (n), TOF for HER and OER was calculated by following Eqs (S6) and (S7), respectively.

For HER:

$$TOF = \frac{I}{2nF} \quad \text{(S6)}$$

For OER:

$$TOF = \frac{I}{4nF} \quad \text{(S7)}$$

Where, I the current density measured by the LSV plots in 1.0 M KOH for HER and OER.[5,6]

The electrochemical active surface area (ECSA) can be calculated by using the equation (Eq S8):

$$ECSA = {C_{dl}}/{C_e} \quad \text{(S8)}$$

Where C_{dl} is the double layer capacitance and Ce is the specific capacitance of the alkaline electrolyte and for 1.0 M KOH had a specific capacitance of 0.04 mF cm^{-2}. No iR compensation was applied to the polarization curves, and all overpotentials reported in this study are uncorrected data.

Characterization techniques

The Fourier transform infrared spectroscopy (FT-IR) was used to study the vibrational frequency of the as-prepared electrocatalysts using a Bruker TENSOR 27 spectrometer in the scanning range of 400–4000 cm^{-1}. The crystallographic nature of the as-prepared composites was measured by Powder X-ray diffractometer (PXRD) (PANalytical) with Cu Ka irradiation (1.5406 Å) with an angle range of 2θ = 5 - 85°. The composition and chemical states of the synthesized composite were elucidated by X-ray photoelectron spectroscopy (XPS) using PHI Versa Probe III, Software Version: SS 2.7.1.22. Brunauer-Emmett-Teller (BET) surface area analysis using N_2 adsorption/desorption isotherm and Barrett-Joyner-Halenda (BJH) pore size and volume analysis of the nanocomposites were carried out using Quanta Chrome Instruments, USA, ASiQ win Version 5.0 (1994-2016). Scanning electron microscopy (SEM) (VEGA3, TESCAN (Czech Republic)) was used to study the nanostructure of the as-prepared composite materials. The elemental composition of the prepared materials was identified

using an energy dispersive X-ray spectrometer (EDAX) (BRUKER Nano, GmbH, D-12489 (Germany)) with an accelerating voltage of 0 to 30 KeV. High-resolution transmission electron microscopy (HR-TEM) (JEOL Japan, JEM-2100 Plus (operating voltage 200 kV)) was used to examine the structural morphology of the as-prepared nanocomposites. Electrochemical studies such as cyclic voltammetry, linear sweep voltammetry, and impedance spectroscopic techniques were carried out using the Autolab multichannel potentiostat/galvanostat electrochemical workstation (AUT.MAC204.S, Netherlands).

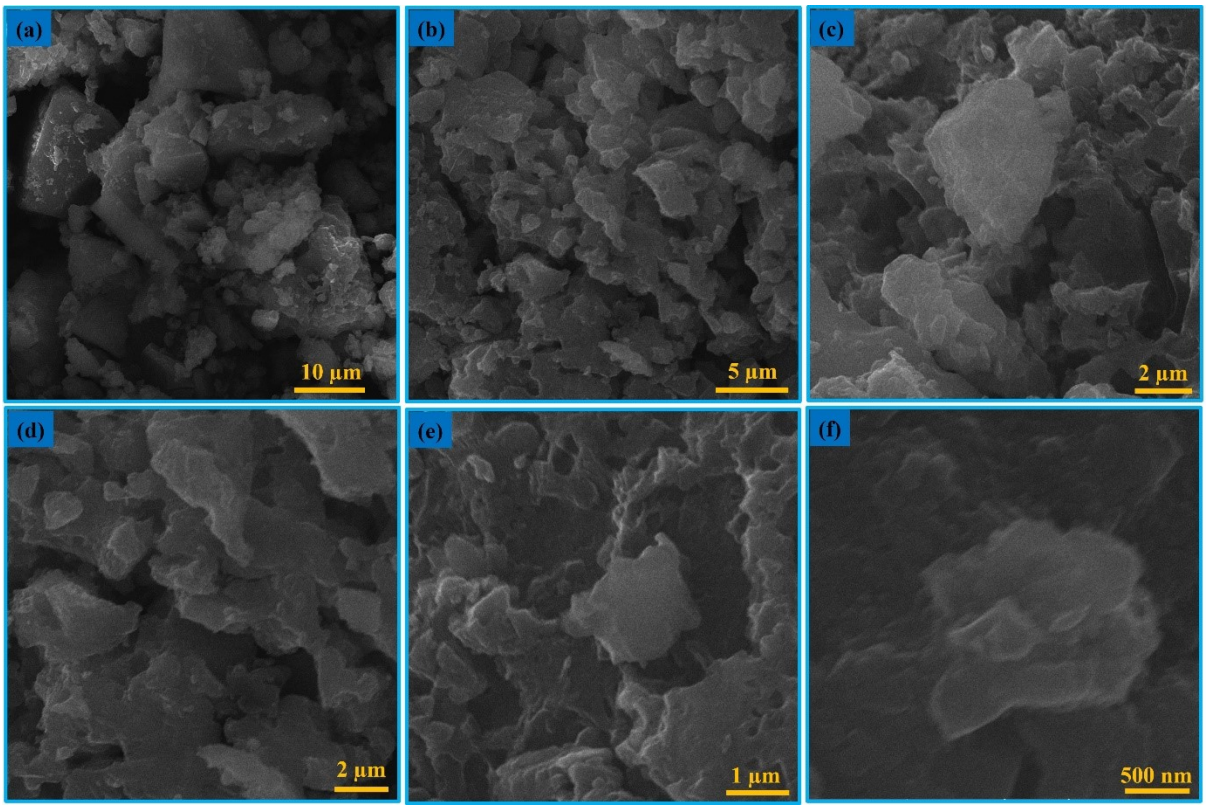

Fig. S1 SEM images of MnS@Al_2S_3@C nanostructure at different magnifications.

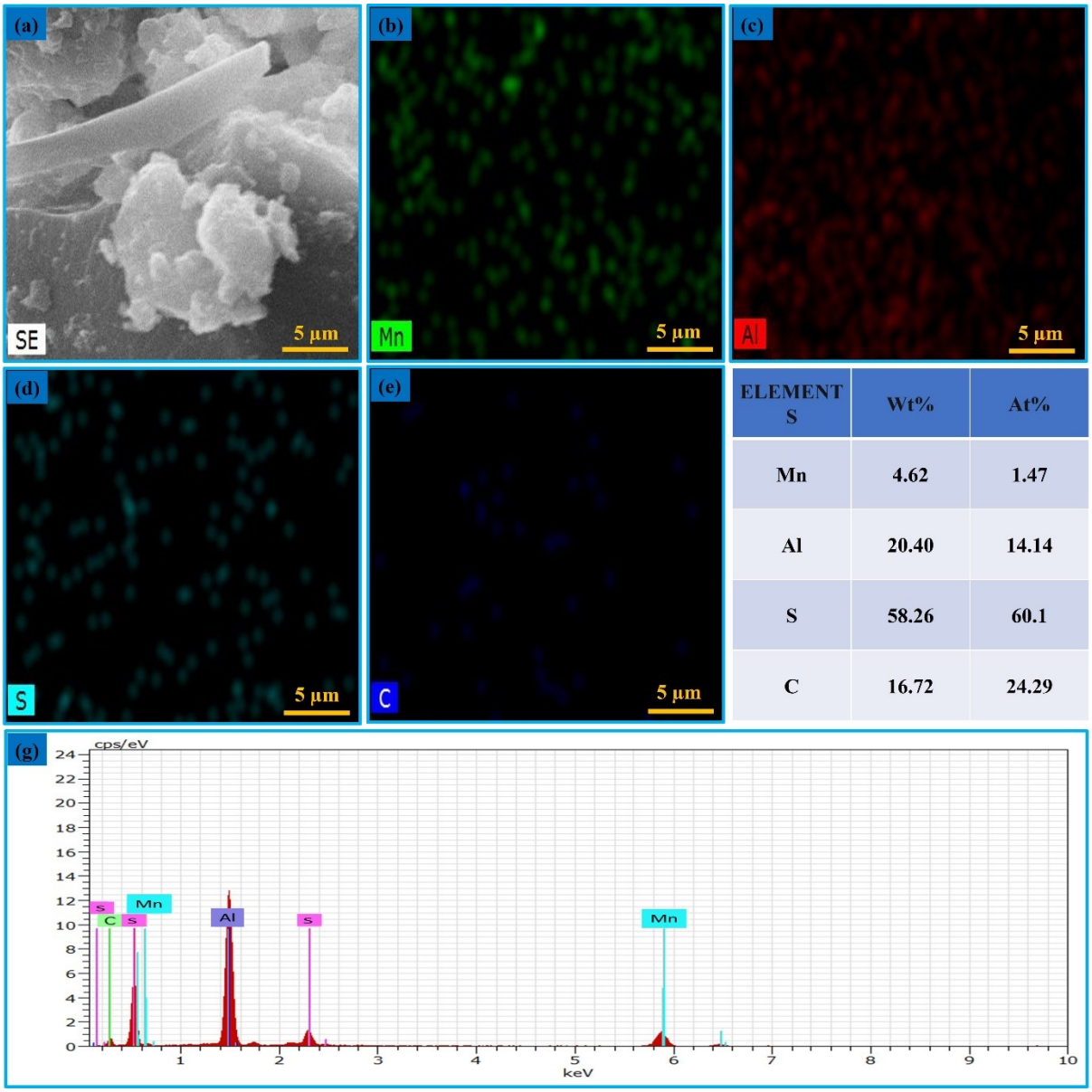

ELEMENTS	Wt%	At%
Mn	4.62	1.47
Al	20.40	14.14
S	58.26	60.1
C	16.72	24.29

Fig. S2 (a) Elemental mapping of the MnS@Al_2S_3@C nanostructures and individual elemental mapping of (b) Mn, (c) Al, (d) S, (e) C, (f) the corresponding weight and atomic percentages and (g) EDAX analysis of the MnS@Al_2S_3@C nanostructures.

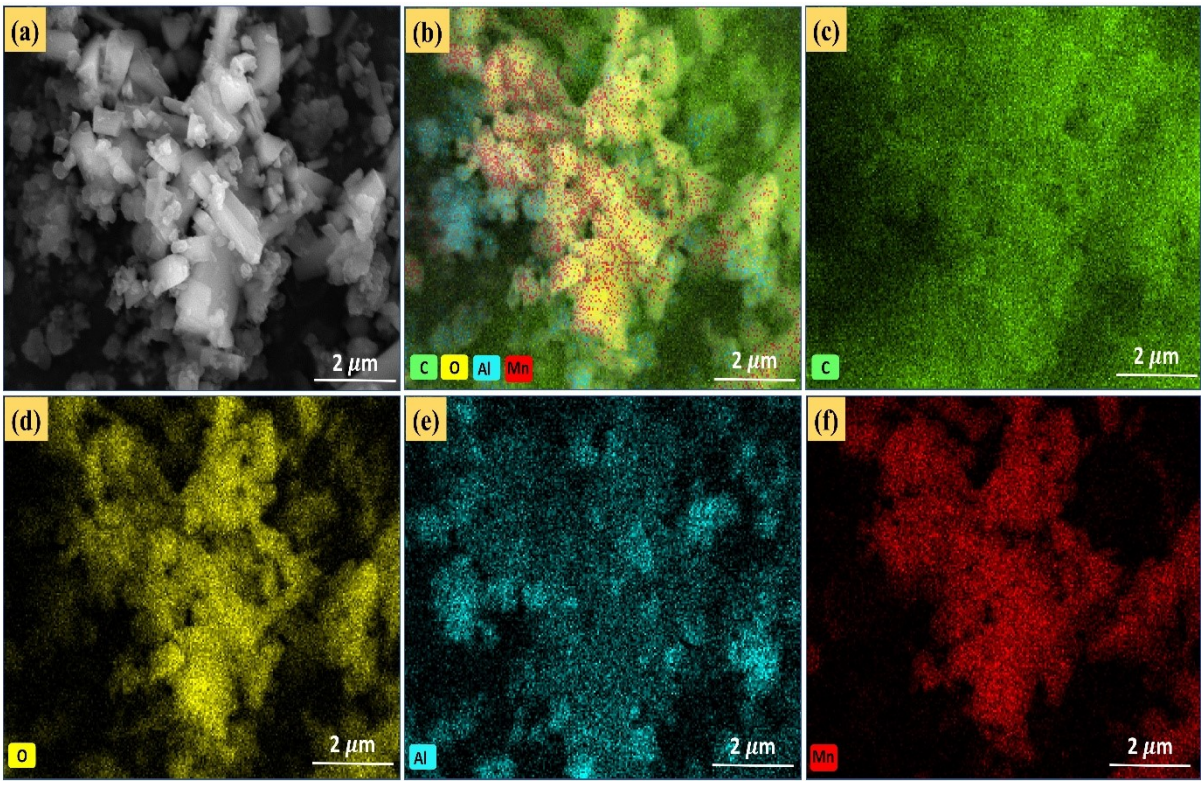

Fig. S3 (a) SEM image, (b) Elemental mapping of the Mn-MOF@Al-MOF and individual elemental mapping of (c) C, (d) O, (e) Al, (f) Mn.

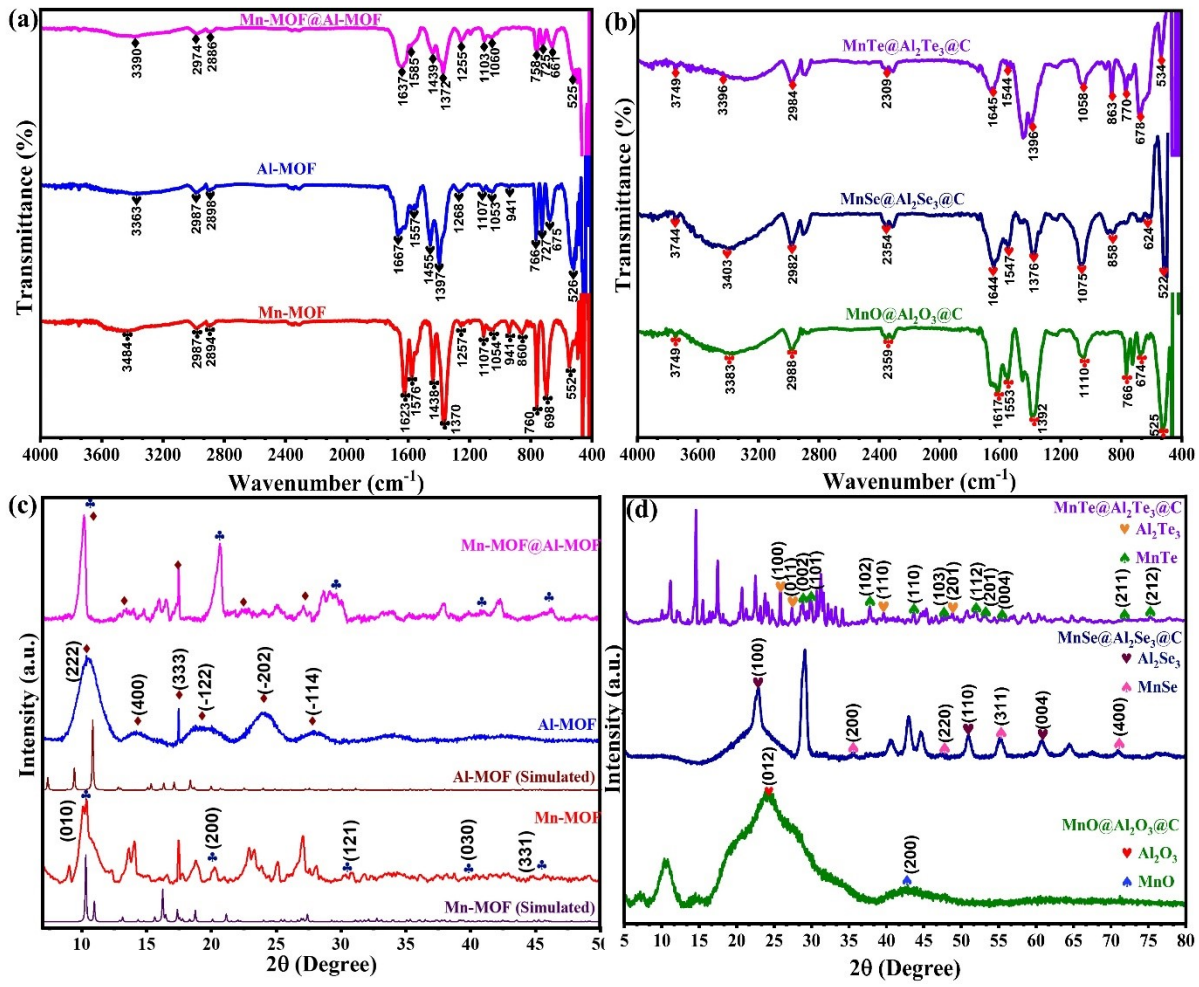

Fig. S4 (a, b) FT-IR spectra, (c) XRD patterns of Mn-MOF, Al-MOF with the corresponding simulated pattern and Mn-MOF@Al-MOF. (d) XRD patterns of the derived MOFs such as $MnO@Al_2O_3@C$, $MnSe@Al_2Se_3@C$ and $MnTe@Al_2Te_3@C$ nanostructures.

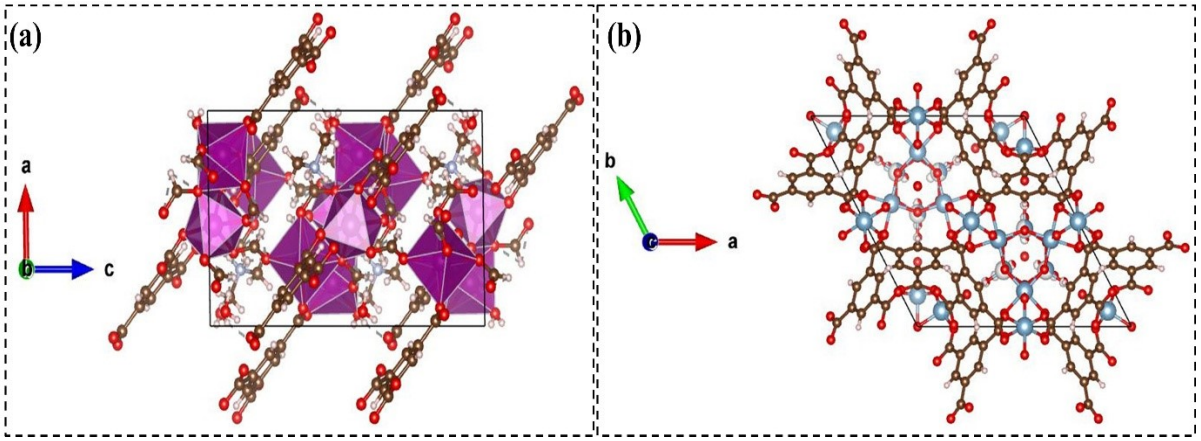

Fig. S5 Crystal structure of (a) Mn-MOF, and (b) Al-MOF.

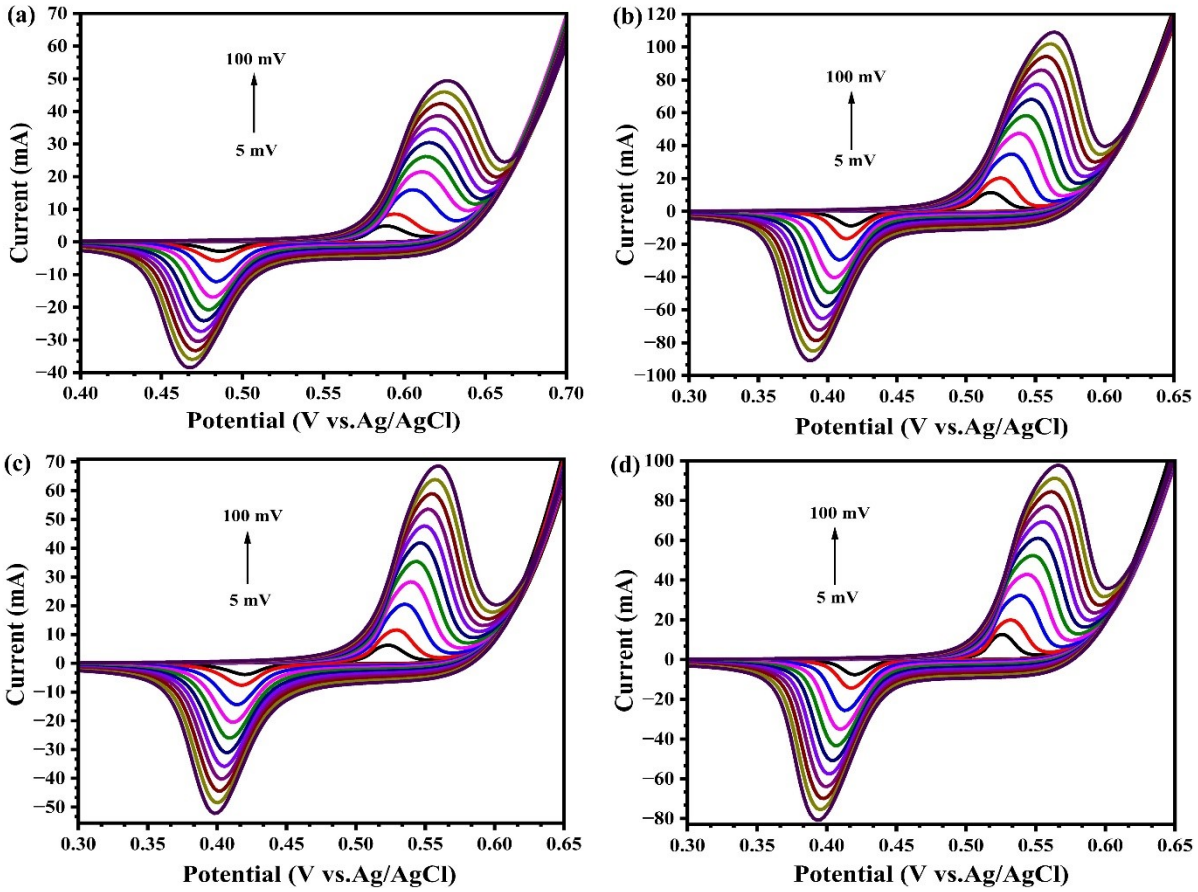

Fig. S6 CVs recorded for (a) bare SS mesh, (b) Mn-MOF, (c) Al-MOF and (d) Mn-MOF@Al-MOF loaded SS mesh electrodes with increasing scan rates from 5 to 100 mV s^{-1} in 1.0 M KOH.

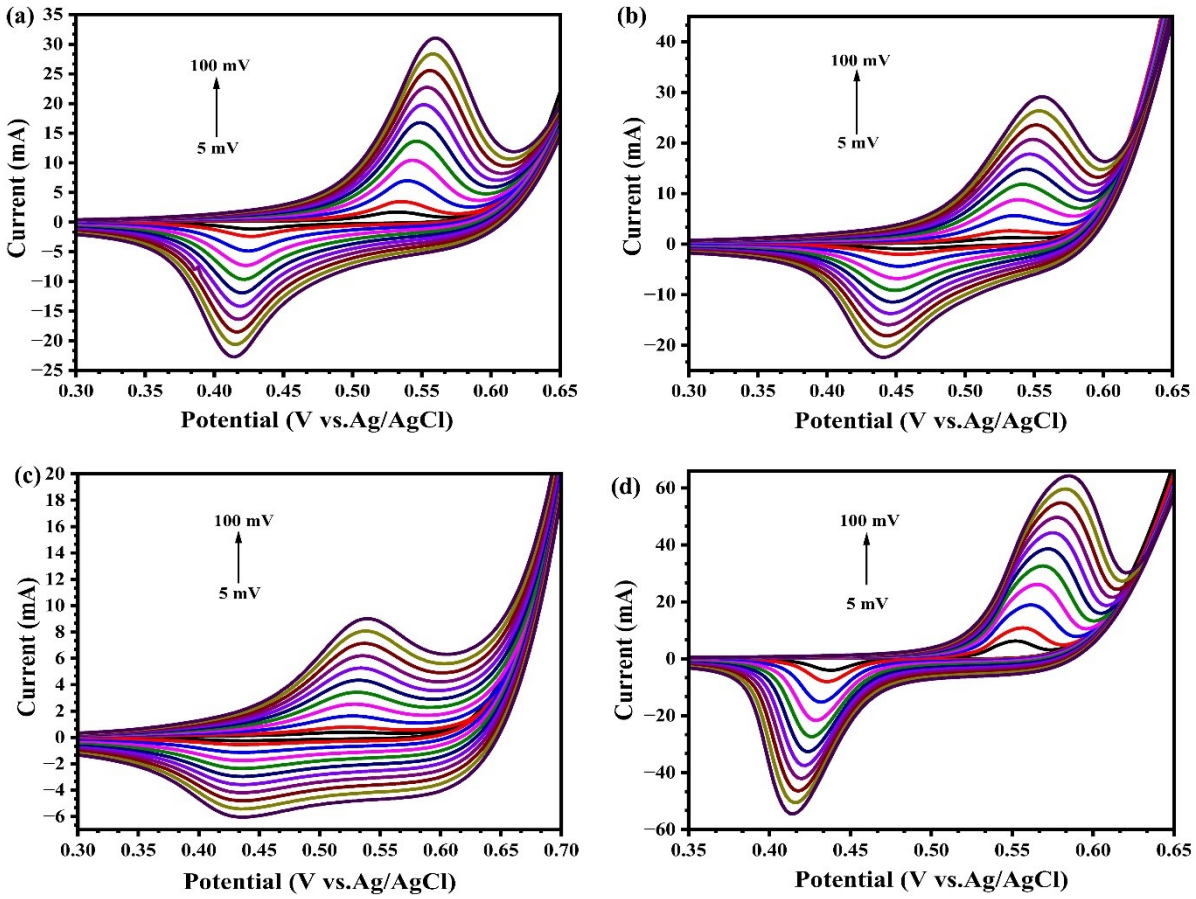

Fig. S7 CVs recorded for (a) $MnO@Al_2O_3@C$, (b) $MnSe@Al_2Se_3@C$, (c) $MnTe@Al_2Te_3@C$ and (d) $MnS@Al_2S_3@C$ loaded SS mesh electrodes with increasing scan rates from 5 to 100 mV s^{-1} in 1.0 M KOH.

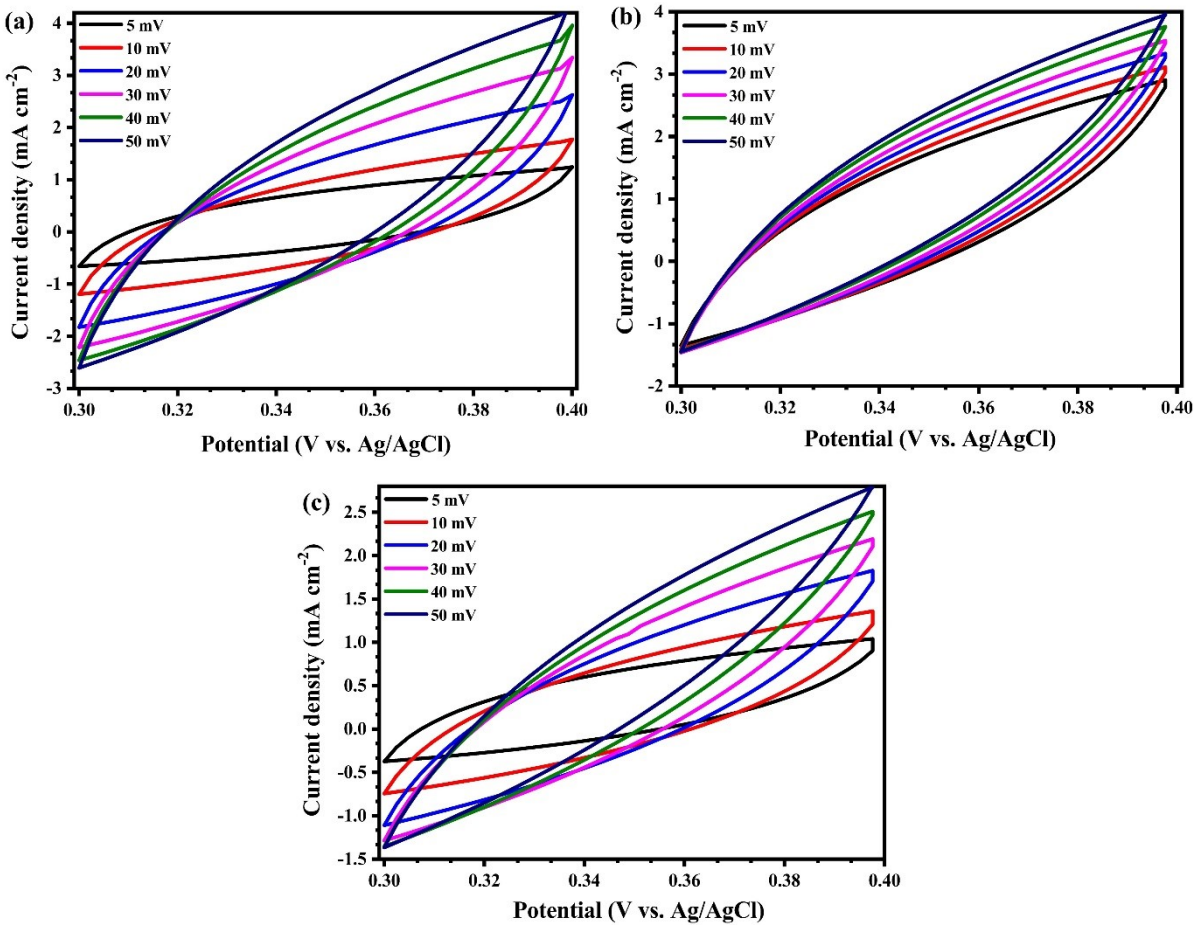

Fig. S8 CVs recorded for (a) Mn-MOF, (b) Al-MOF and (c) Mn-MOF@Al-MOF in the non-faradaic region at the same potential range with increasing scan rates in 1.0 M KOH.

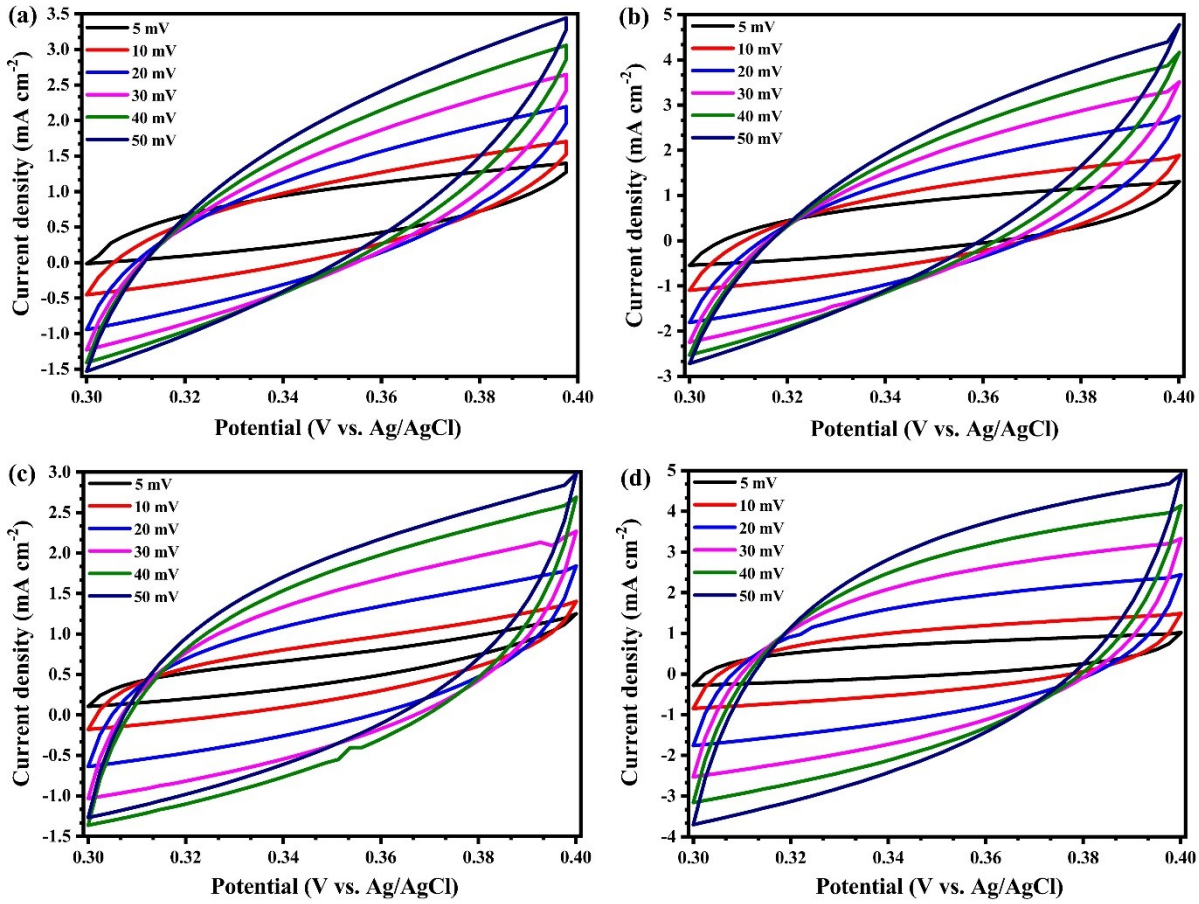

Fig. S9 CVs recorded for (a) $MnO@Al_2O_3@C$, (b) $MnSe@Al_2Se_3@C$, (c) $MnTe@Al_2Te_3@C$ and (d) $MnS@Al_2S_3@C$ in the non-faradaic region at the same potential range with increasing scan rates in 1.0 M KOH.

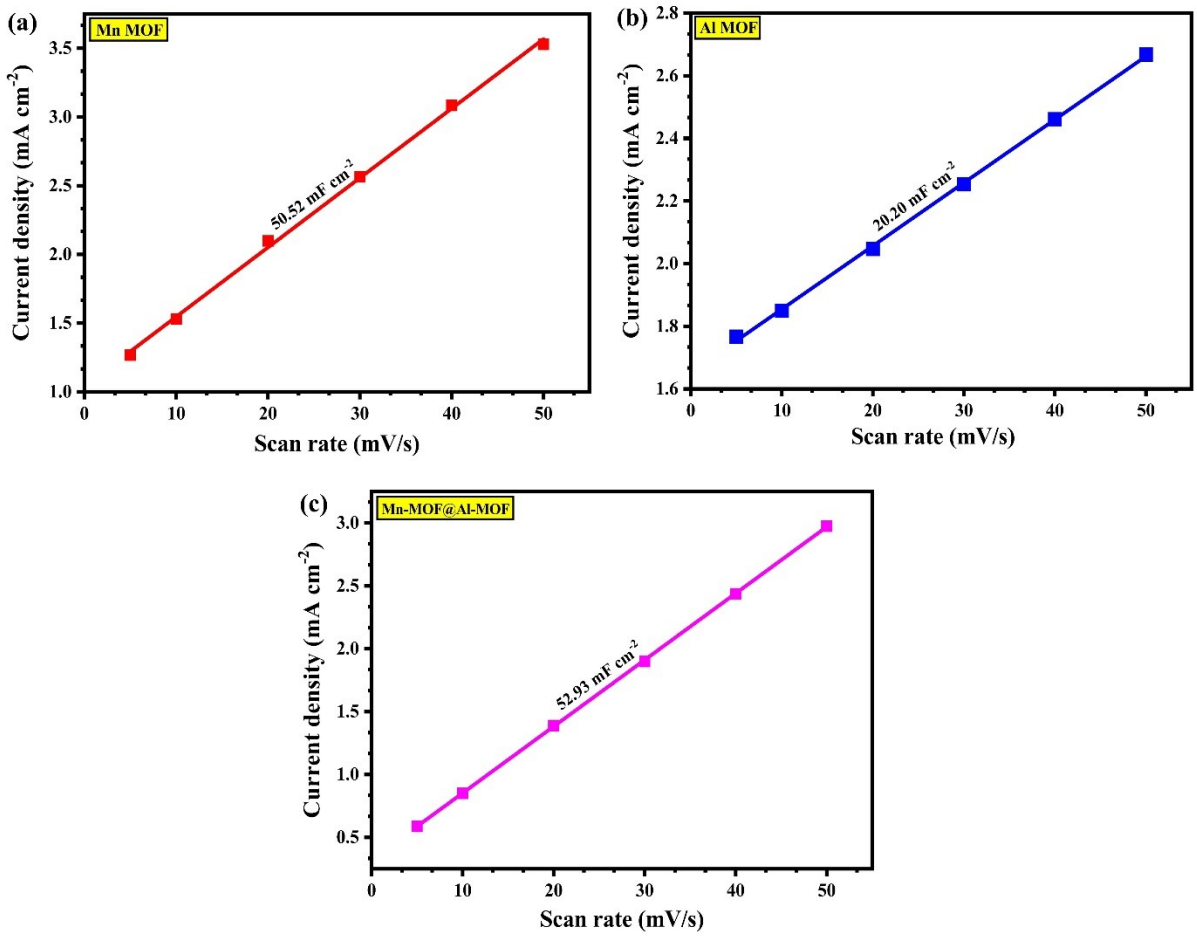

Fig. S10 Capacitive current densities (vs. RHE) derived from CVs against scan rates for (a) Mn-MOF, (b) Al-MOF and (c) Mn-MOF@Al-MOF nanostructures.

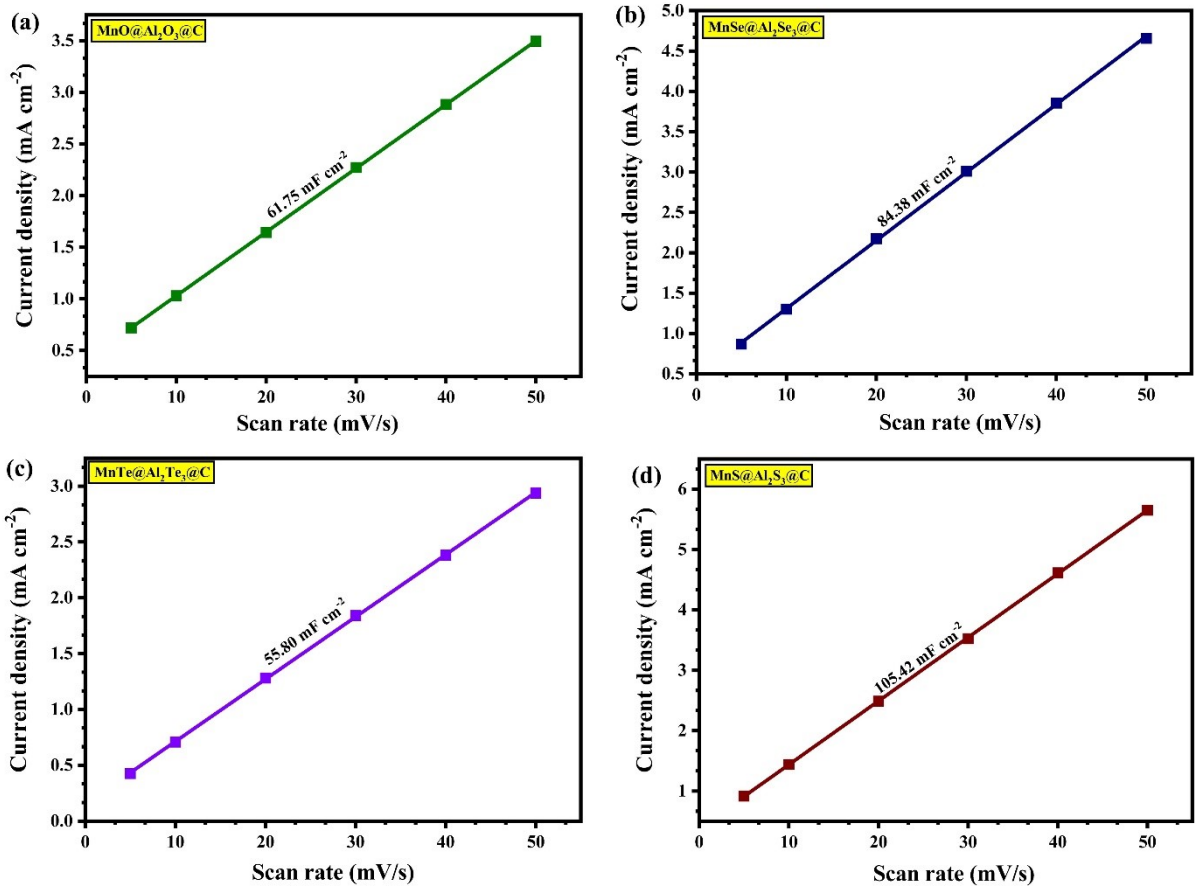

Fig. S11 Capacitive current densities (vs. RHE) derived from CVs against scan rates for (a) MnO@Al_2O_3@C, (b) MnSe@Al_2Se_3@C, (c) MnTe@Al_2Te_3@C and (d) MnS@Al_2S_3@C nanostructures.

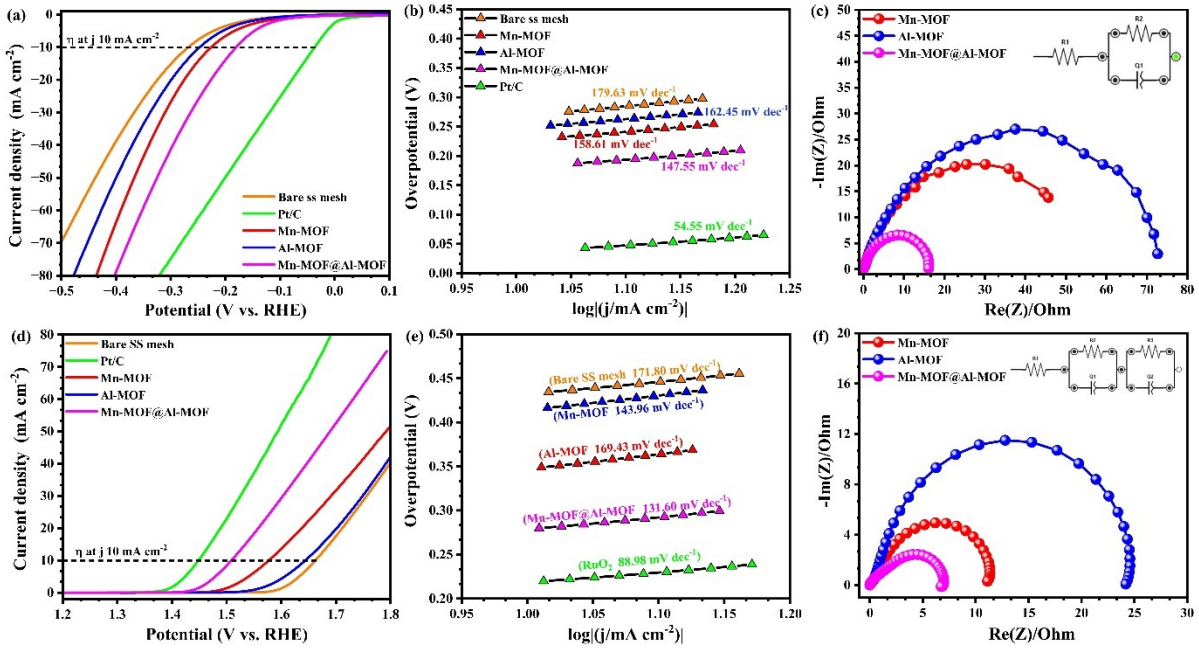

Fig. S12 (a, d) The LSV polarization curves (b, e) Tafel plots and (c, f) EIS curves with equivalent circuit in the inset showing the HER and OER performances, respectively corresponding to Mn-MOF, Al-MOF and Mn-MOF@Al-MOF in 1.0 M KOH.

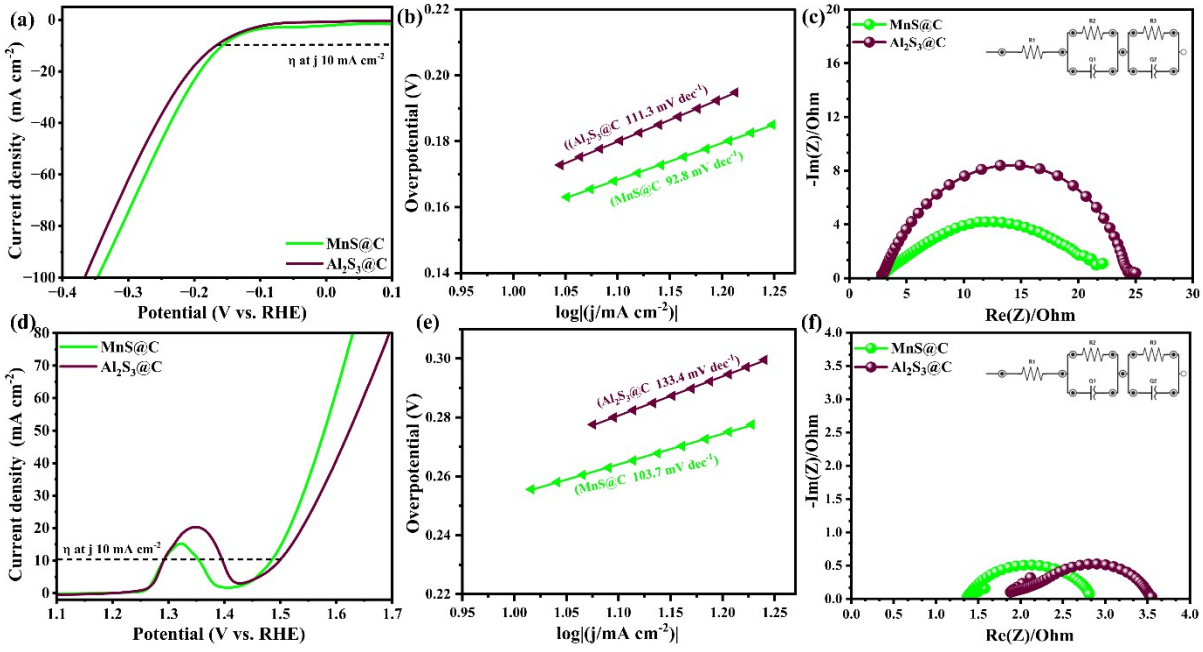

Fig. S13 (a, d) The LSV polarization curves (b, e) Tafel plots and (c, f) EIS curves with equivalent circuit in the inset showing the HER and OER performances, respectively corresponding to MnS@C and Al_2S_3@C in 1.0 M KOH.

Plausible HER Mechanism of MnS@Al_2S_3@C nanostructures

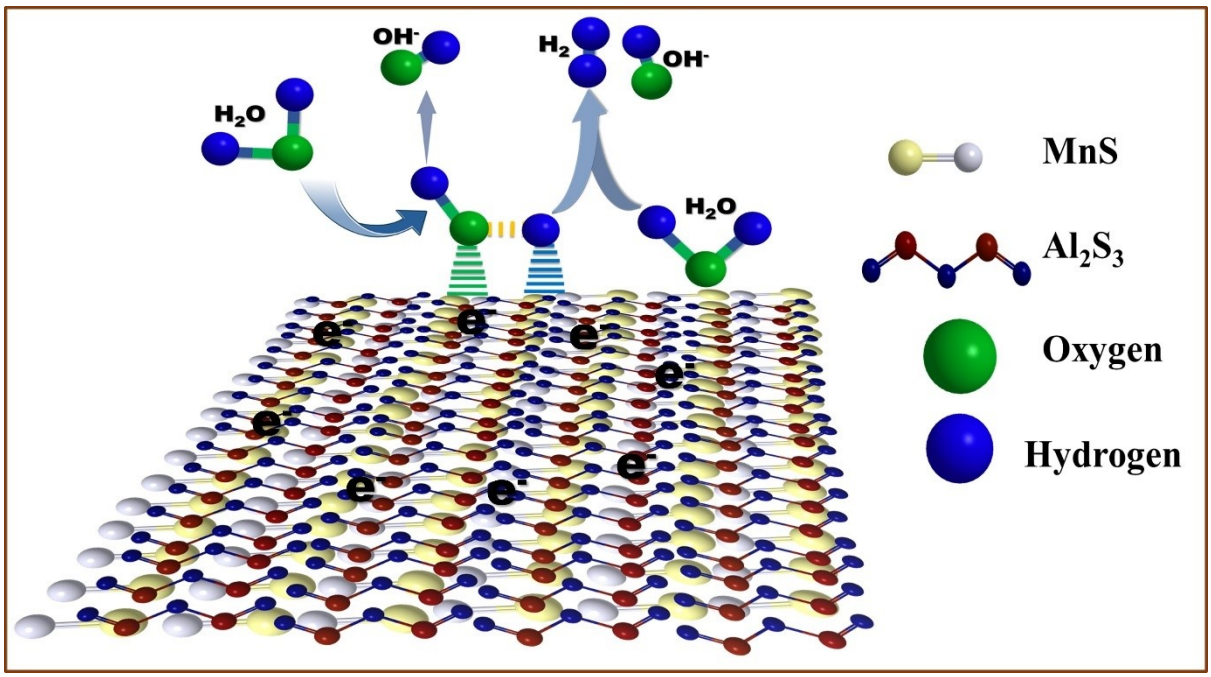

Fig. S14 Schematic representation of HER mechanism at MnS@Al_2S_3@C nanostructures.

HER is a two-electron transfer process involving multiple steps. Eqs (S9) – (S11) showed the mechanisms of the HER reaction, and the X*, and H_{ads} represent the MnS@Al_2S_3@C catalytic sites and the adsorbed hydrogen on the catalyst surface.

$$H_2O + e^- + X^* \rightarrow X^* - H_{ads} + OH^- \quad \text{(Volmer step)} \qquad \text{(S9)}$$

$$X^* - H_{ads} + H_2O + e^- \rightarrow H_2 + X^+ + OH^- \quad \text{(Heyrovsky step)} \qquad \text{(S10)}$$

$$X^* - H_{ads} + H_{ads} - X^* \rightarrow H_2 + 2X^* \quad \text{(Tafel step)} \qquad \text{(S11)}$$

The dissociation of water to form adsorbed hydrogen which then converted to gaseous dihydrogen (H_2) is the cathodic reaction of water electrolysis in alkaline electrolytes. After taking into account, Fig. S14 and elementary steps mentioned above, it is evident that there are two distinct reaction pathways that result in the formation of HER: the Volmer–Heyrovsky and Volmer–Tafel mechanisms. In both cases, the first step involves an adsorbed hydrogen atom built on the surface of the catalyst by the adsorption of a proton on the

catalyst surface and represented as H_{ads}. This step is called as Volmer step. There are two alternative pathways followed by the Volmer process, the H_{ads} would incline to couple with another H^+ ion and electrons to form an H_2 molecule in the case of low coverage of H_{ads} on the catalyst surface, where this step is called the Heyrovsky step. On an alternative route, when the coverage of H_{ads} was high, two adjacent H_{ads} atoms bind to form an H_2 molecule and this step is called the Tafel step. H_{ads} seems to be the only reaction intermediate whose adsorption strength has been recognized as the controlling factor with respect to the elementary stages of HER.[7–9]

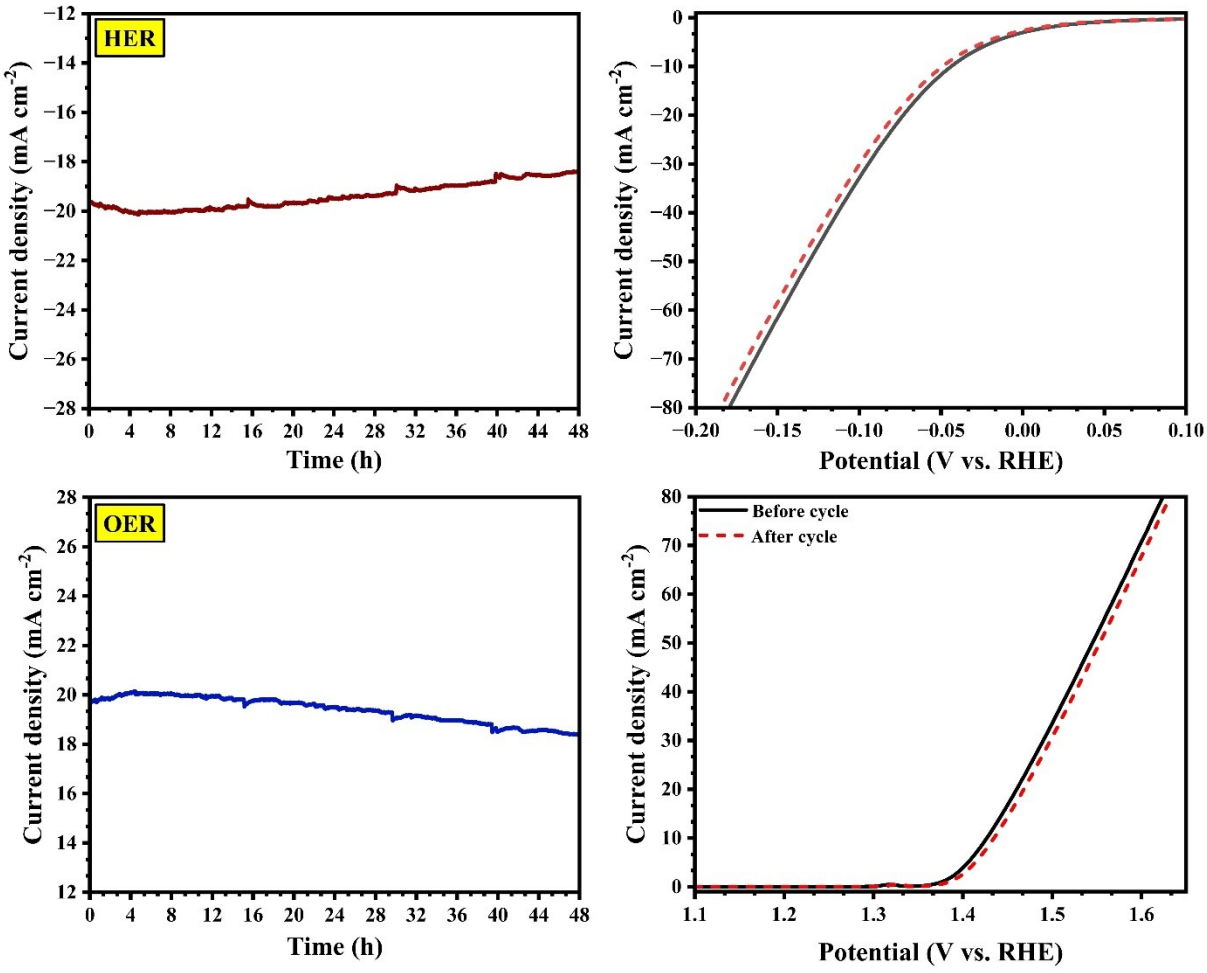

Fig. S15 Chronoamperometric stability study of $MnS@Al_2S_3@C$ for 48 h at a constant potential with corresponding LSV polarization curves of the electrocatalyst before and after chronoamperometry study for 48 h for (a, b) HER and (c, d) OER performances, respectively.

Plausible OER Mechanism of MnS@Al_2S_3@C nanostructures

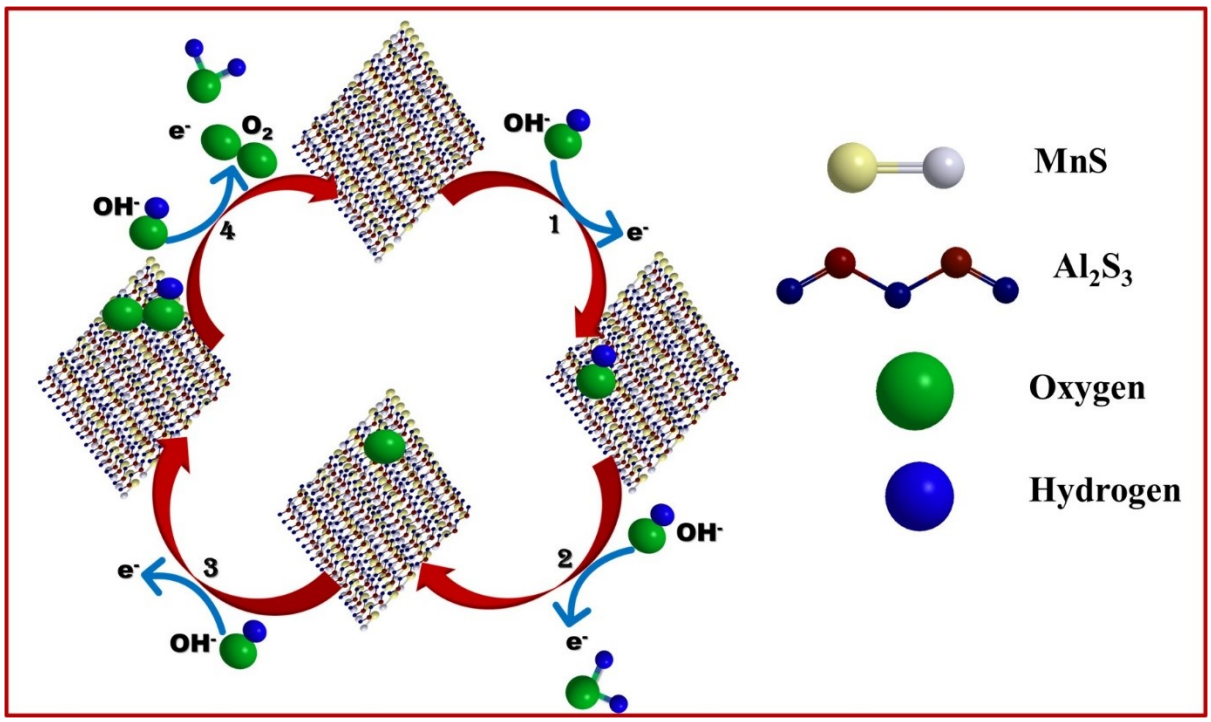

Fig. S16 Schematic illustration of the OER mechanism at MnS@Al_2S_3@C nanostructures.

Typically, OER is more kinetically sluggish compared to HER. OER is associated with a complex four-electron transfer process that involves the difficult O-O bond formation and O-H bond cleavage, and these steps significantly hinder the water electrolysis efficiency. Eqs S12 – S16 displayed the well-accepted OER mechanisms in the alkaline solution, where *stands for the catalytic site on the electrocatalyst surface. The hydroxyl ion is gradually transformed into the intermediates of X^*OH, X^*O and X^*OOH via proton-coupled electron-transfer steps in an alkaline electrolyte. The combination of Al and Mn within the electrocatalyst results in the formation of oxyhydroxide X^*OOH in alkaline electrolyte, leading to the production of O_2 gas through its reaction with OH^- ions (Fig. S16). Thus, the adsorbate evolution mechanism (AEM) was followed at MnS@Al_2S_3@C nanostructure for the generation of O_2 molecules through anodic OER. The reaction proceeds as follows:

$$X^* + OH^- \rightarrow X^*OH + e^- \quad \text{(S12)}$$

$$X^*OH + OH^- \rightarrow X^*O + H_2O + e^- \quad \text{(S13)}$$

$$X^*O + X^*O \rightarrow O_2 + 2X^* \quad \text{(S14)}$$

$$X^*O + OH^- \rightarrow X^*OOH + e^- \quad \text{(S15)}$$

$$2X^*OOH + OH^- \rightarrow 2X^* + O_2 + H_2O + e^- \quad \text{(S16)}$$

(i) In the first step, by one-electron oxidation, the hydroxyl anion (OH^-) from the electrolyte was adsorbed on the active site (X^*) to give X^*OH (*represents the adsorption of the O-intermediate on X) (Eq S12).

(ii) In the second step, the intermediate X^*O was formed by the combination of X^*OH with another hydroxyl ion (OH^-) with the release of an electron and a water molecule. This was the rate-limiting step that determines the overpotential of the electrocatalyst with respect to the binding strengths of O^- and OH^- (Eq S13).

(iii) In the third step, the X^*O was converted into X^*OOH intermediate by the attack of OH^- by the adsorbed oxygen (Eqs S14, S15)

(iv) Finally, the O_2 molecule was produced by the reaction intermediate X^*OOH with another OH^- with the release of a water molecule. (Eq S16)

The KOH electrolyte with several OH^- ions was adsorbed at the active metal sites of MnS@Al_2S_3@C nanostructure and formed lattice oxygen via the bridging mode. This lattice oxygen was then further attacked by OH^- ions to directly form O–O bonds to produce O_2

molecules (Eq S14). To ensure a delicate balance between the adsorption and desorption processes, the adsorption strength of the reaction intermediates to the catalytic sites should not be too strong or too weak. The active sites of MnS@Al_2S_3@C nanostructure were located on edge or defect sites that have a coordination number of less than six and three for the metal and oxygen sites, respectively, and thus have proper adsorption energies for OER intermediates. Compared to HER, OER is a more complicated process that involves the participation of intermediates (OH* and OOH*) at various stages. The repulsion between the S 3p and O 2p orbitals plays a crucial role in preventing the coordination of X^*OH with metal atoms by electronegative S atoms in MnS@Al_2S_3@C. Additionally, the formation of the X^*OOH intermediate may be facilitated by the delocalized electrons of the S atom, and the repulsion between the S 3p and O 2p orbitals can accelerate the oxidation of the intermediate. This conversion of MnS@Al_2S_3@C to metal hydrogen is a critical step in the OER process.[9–11]

Further, under alkaline OER conditions, transition-metal sulfides are prone to surface oxidation and anion exchange. In the MnS@Al_2S_3@C system, anodic polarization induces partial sulfur leaching and the formation of MnOOH/MnOx species on the surface. These in situ-generated high-valence Mn species (Mn^{3+}/Mn^{4+}) are widely recognized as the actual active centers for oxygen evolution. Therefore, MnS acts as a precatalyst that dynamically reconstructs into catalytically active oxyhydroxide phases, while the Al_2S_3 and carbon matrix maintain structural integrity and electronic conductivity.[12]

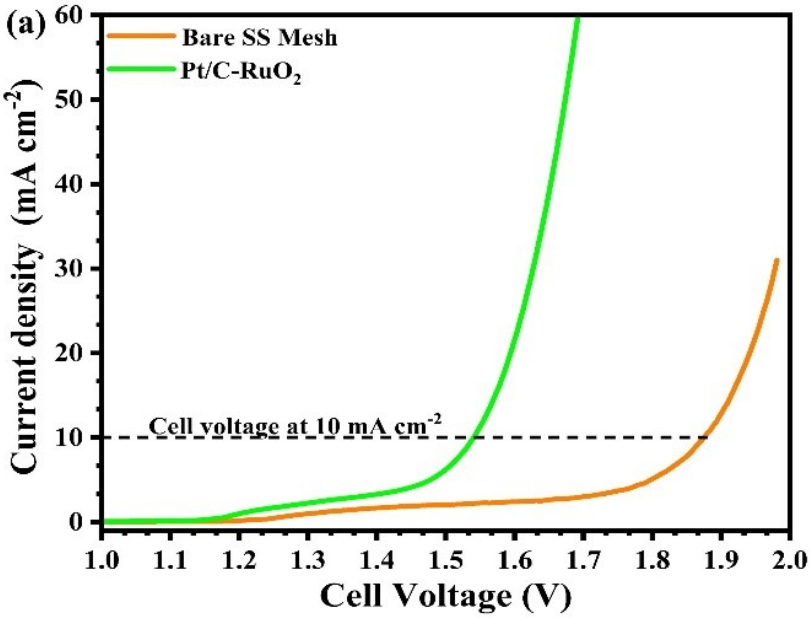

Fig. S17 LSV polarization curves showing the overall water splitting performance of bare SS mesh and Pt/C//RuO_2 loaded electrode in 1.0 M KOH.

Table S1 The charge transfer resistance (R_{ct}) of the electrocatalyst for HER, OER, and overall water splitting.

Composites	HER (Ω)	OER (Ω)	OWS (Ω)
Mn-MOF	47.00	11.12	-
Al-MOF	72.64	24.19	-
MnS@C	18.30	1.41	-
Al_2S_3@C	22.40	1.75	-
Mn-MOF@Al-MOF	16.00	6.74	-

$MnO@Al_2O_3@C$	12.90	5.99	12.12
$MnSe@Al_2Se_3@C$	12.35	1.26	10.28
$MnTe@Al_2Te_3@C$	13.82	7.20	12.80
$MnS@Al_2S_3@C$	4.72	1.15	8.03

Table S2 Comparison of electrochemical activity of $MnS@Al_2S_3@C$ nanostructure with recently reported similar type of nanomaterials.

S. No	Electrocatalyst	Electrolyte	OER, η(mV)@10 mA cm^{-2}	HER, η(mV)@10 mA cm^{-2}	Cell voltage (V)	Stability (h)	Ref.
1	$CoTe_2@CdTe$	1.0 M KOH	140	110	1.51	8.33	[13]
2	$Co_3S_4@MoS_2$	1.0 M KOH	280	136 1.0 M H_2SO_4	1.58	10	[14]
3	NiFeSP/NF	1.0 M KOH	240	91	1.58	20	[15]
4	Ni_3S_2	1.0 M KOH	295	112	1.63	108	[16]
5	$CoMnS_2$@1T-Fe-VS_2@NF	1.0 M KOH	260	89	1.51	40	[17]
6	NF/T(Ni_3S_2/MnS-O)	1.0 M KOH	228	116	1.54	50	[12]
7	$MnCo_2S_4$-MoS_2/NF	1.0 M KOH	220	105	1.49	20	[18]
8	Se-MnS/NiS	1.0 M KOH	211	56	1.47	48	[19]
9	MnS_xSe_{1-x}@N,F-CQD	1.0 M KOH	209	87	1.55	96	[20]
10	HMS/MoS_2/Co_9S_8	1.0 M KOH	200	85	1.56	10	[21]

	/P-31						
11	NIM-150	1.0 M KOH	250	248	1.69	22	[22]
12	NiFeS/NF	1.0 M KOH	210	75	1.46	50	[23]
13	**MnS@Al_2S_3@C**	**1.0 M KOH**	**196**	**44**	**1.49**	**100**	**This work**

References

1 A. Gowrisankar, K. Selvadharshini, K. M. Nair and T. Selvaraju, *New Journal of Chemistry*, 2023, 47, 9819–9832.

2 G. Aruchamy and S. Thangavelu, *Electrochim Acta*, DOI:10.1016/j.electacta.2020.136141.

3 A. Gowrisankar and T. Selvaraju, *Langmuir*, 2021, 37, 5964–5978.

4 K. M. Nair, G. Aruchamy and S. Thangavelu, *Journal of Electroanalytical Chemistry*, DOI:10.1016/j.jelechem.2023.117968.

5 K. M. Nair, P. Shankar and S. Thangavelu, *Dalton Transactions*, DOI:10.1039/d4dt02542c.

6 S. Riyajuddin, K. Azmi, M. Pahuja, S. Kumar, T. Maruyama, C. Bera and K. Ghosh, *ACS Nano*, 2021, 15, 5586–5599.

7 S. Baiju, M. U., S. Datta, K. Tarefder, J. Chaturvedi, S. Ramakrishna and L. N. Tripathi, *Int J Hydrogen Energy*, 2024, 51, 779–808.

8 K. M. Nair, S. Kanthasamy, G. Aruchamy and S. Thangavelu, *Langmuir*, DOI:10.1021/acs.langmuir.4c04577.

9 Y. J. Son, K. Kawashima, R. A. Márquez, L. A. Smith, C. E. Chukwuneke and C. B. Mullins, *Curr Opin Electrochem*, 2023, 39, 101298.

10 G. Aruchamy, S. Kanthasamy, B.-K. Kim and S. Thangavelu, *Electrochim Acta*, 2024, 507, 145190.

11 C. Wang, Y. Lin, L. Cui, J. Zhu and X. Bu, *Small*, DOI:10.1002/smll.202207342.

12 Y. Zhang, J. Fu, H. Zhao, R. Jiang, F. Tian and R. Zhang, *Appl. Catal. B*, 2019, 257, 117899.

13 K. Chandra Majhi, P. Karfa and R. Madhuri, *Electrochim. Acta*, 2019, 318, 901–912.

14 Y. Guo, J. Tang, Z. Wang, Y.-M. Kang, Y. Bando and Y. Yamauchi, *Nano Energy*, 2018, 47, 494–502.

15 Y. Xin, X. Kan, L.-Y. Gan and Z. Zhang, *ACS Nano*, 2017, 11, 10303–10312.

16 X. Zheng, X. Han, Y. Zhang, J. Wang, C. Zhong, Y. Deng and W. Hu, *Nanoscale*, 2019, 11, 5646–5654.

17 P. P. Dhakal, U. N. Pan, D. R. Paudel, M. R. Kandel, N. H. Kim and J. H. Lee, *Mater. Today Nano*, 2022, 20, 100272.

18 J. Gautam, D. Chanda, M. Mekete Meshesha, S. G. Jang and B. Lyong Yang, *J Colloid Interface Sci*, 2023, 638, 658–671.

19 J. Zhu, M. Sun, S. Liu, X. Liu, K. Hu and L. Wang, *J Mater Chem A*, 2019, 7, 26975–26983.

20 B. Sun, G. Dong, J. Ye, D. Chai, X. Yang, S. Fu, M. Zhao, W. Zhang and J. Li, *Chem. Eng. J.* 2023, 459, 141610.

21 F. Amiripour and S. Ghasemi, *Fuel*, 2023, 346, 128299.

22 P. C. Nagajyothi, K. Pavani, R. Ramaraghavulu and J. Shim, *Int. J Hydrogen Energy*, 2024, 54, 691–699.

23 L. Meng, H. Xuan, J. Wang, X. Liang, Y. Li, J. Yang and P. Han, *Int. J. Hydrogen Energy*, 2024, 51, 271–280.